Applied Catalysis B: Environmental 233 (2018) 80–87

Contents lists available at ScienceDirect

Applied Catalysis B: Environmental

journal homepage: www.elsevier.com/locate/apcatb

Rapid high-temperature treatment on graphitic carbon nitride for excellent photocatalytic H_2-evolution performance

Yazhou Zhang, Shichao Zong, Cheng Cheng, Jinwen Shi*, Penghui Guo, Xiangjiu Guan, Bing Luo, Shaohua Shen, Liejin Guo

International Research Center for Renewable Energy (IRCRE), State Key Laboratory of Multiphase Flow in Power Engineering (MFPE), Xi'an Jiaotong University (XJTU), 28 West Xianning Road, Xi'an, 710049, China

ARTICLE INFO

Keywords:
Nanosheet
Thermal treatment
Porous structure
Nitrogen vacancy
Visible light

ABSTRACT

Graphitic carbon nitride is considered as one of the most potential photocatalysts for utilizing solar energy. Herein, an efficient route of rapid high-temperature treatment (at 800 °C in air for 0–20 min) was developed to modify pristine graphitic carbon nitride. It was found that, after rapid high-temperature treatment, the obtained photocatalysts showed greatly enhanced photocatalytic H_2-evolution activities (around 25.5 times) under visible-light irradiation attributed to the following reasons. More active sites for photocatalytic reaction were provided by the significant increase of surface areas. The generation, separation and transfer of photo-generated carriers were effectively promoted by the quantum confinement effect of thinner graphitic carbon nitride sheets and by the generated nitrogen vacancies in C—N heterocyclic units. Moreover, stronger driving force for photocatalytic H_2-evolution reaction was obtained to enhance the ability of water reduction reaction.

1. Introduction

Semiconductor-based photocatalysis, as one of promising methods to utilize abundant solar energy, has been widely developed, and photocatalytic water reduction for H_2 evolution is considered as the possible way to solve energy crisis [1–3]. Until now, among many kinds of discovered photocatalysts, graphitic carbon nitride has been deeply investigated due to a series of advantages such as metal-free elements, high thermal stability, suitable band structures and favorable chemical stability [4–9]. Generally, graphitic carbon nitride is synthesized by a direct thermal polymerization process starting with corresponding organics such as melamine, urea or thiourea [10,11]. Wang et al. firstly reported photocatalytic performance of graphitic carbon nitride for H_2 evolution under visible-light irradiation in 2009 [4], and furthermore Kang et al. designed the nanocomposite of graphitic carbon nitride and metal-free carbon nanodot for effectively photocatalytic overall water splitting in 2015 [8]. Recently, our group reported a molecular design strategy based on graphitic carbon nitride for efficient H_2 evolution by promoting the exciton dissociation and improving light harvesting ability [9]. However, this material still shows low photocatalytic efficiency mainly due to few active sites induced by low surface areas or high recombination of photo-generated carriers, which badly restricts its application in photocatalysis [12–14].

It is known that graphitic carbon nitride is composed of aggregated two-dimension (2D) sheets, and specific surface areas of perfect monolayer for graphitic carbon nitride might be up to 2500 $m^2 g^{-1}$ by theoretical calculation [10,15]. Meanwhile, only van der Waals exists between adjacent sheets, and thus exfoliation of graphitic carbon nitride sheets is one of the most feasible and effective ways to increase its surface areas and produce more active sites [16,17]. A series of effective exfoliation means, such as mechanical, liquid and thermal exfoliation, have been developed [16,18–21]. However, the complicated process with long duration, high cost or pollution, is adverse for as-reported exfoliation methods.

Due to the 2D structure of graphitic carbon nitride similar to that of graphite [22], exfoliation of graphitic carbon nitride sheets referring to that of graphite-based materials is considered to be feasible. For instance, the Scotch-tape-assisted exfoliation is a traditional way to prepare graphene with thin layers from graphite, and has been successfully used for exfoliation of graphitic carbon nitride [18]. It has been reported that explosive thermal exfoliation is commonly applied to generate porous exfoliated graphene or graphene oxide [23–26]. In the explosive thermal exfoliation process of graphene oxide, high temperature and fast heating rate are two key factors to influence the morphology and surface areas [27–29]. The former is proved to be favorable to exceed the constraint of van der Waals forces between sheets in graphene oxide, and the latter is known to be important to obtain high surface areas [27]. Meanwhile, the explosive thermal

* Corresponding author.
E-mail address: jinwen_shi@mail.xjtu.edu.cn (J. Shi).

https://doi.org/10.1016/j.apcatb.2018.03.104
Received 1 March 2018; Received in revised form 20 March 2018; Accepted 28 March 2018
Available online 29 March 2018
0926-3373/

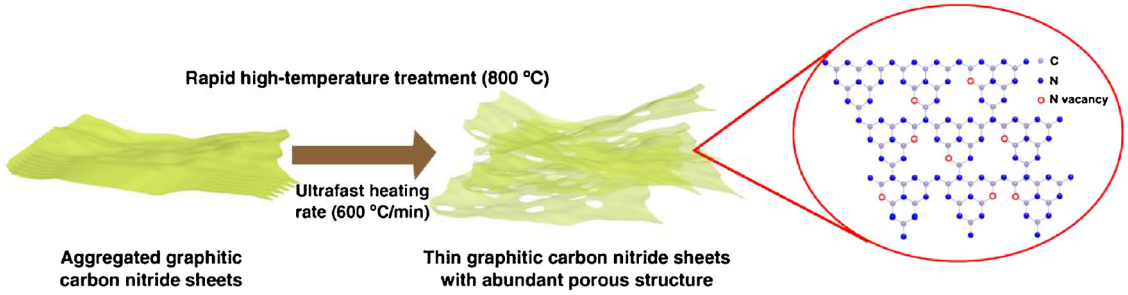

Scheme 1. The preparation process of graphitic carbon nitride with rapid high-temperature treatment.

exfoliation promotes the generation of porous structures [27,28]. Therefore, similar explosive thermal exfoliation for graphitic carbon nitride is speculated to be promising to yield higher surface areas and then generate more active sites for photocatalysis.

Herein, as shown in Scheme 1, following the explosive thermal exfoliation of graphite-based materials, we designed a similar explosive thermal exfoliation of graphitic carbon nitride, that is, the rapid high-temperature treatment. Due to good thermal stability of graphitic carbon nitride up to 600 °C in air atmosphere [30,31], it is necessary to ensure the treated temperature higher than 600 °C for overcoming the van der Waals forces between graphitic carbon nitride sheets. Until now, the reported temperature of thermal treatment on graphitic carbon nitride is commonly lower than 600 °C, and the van der Waals forces between graphitic carbon nitride sheets are partially overcome to realize the thermal exfoliation to some extent [16,17]. If the thermal treatment is carried out at a temperature much higher than 600 °C, it is anticipated that the van der Waals forces could be better conquered for the thermal exfoliation of graphitic carbon nitride. Since the thermal treatment temperature (800 °C) is much higher than 600 °C, graphitic carbon nitride would decompose rapidly. Accordingly, ultrafast heating rate and short duration are necessary to realize the high-temperature treatment and to avoid the complete decomposition of graphitic carbon nitride. The rapid high-temperature treatment shows the merits of short duration, simple operation, and low cost. Based on different kinds of characterization, the influence of rapid high-temperature treatment on physicochemical properties of graphitic carbon nitride, especially its micromorphological and electronic-structure properties, were comprehensively investigated. Moreover, the mechanism of enhanced photocatalytic performance by the rapid high-temperature treatment was deeply analyzed.

2. Experimental section

2.1. Preparation

Pristine graphitic carbon nitride was prepared by thermal condensation of melamine ($C_3H_6N_6$). Briefly, melamine (4.0 g) was added into a corundum crucible, and heated up to 520 °C with a heating rate of 5 °C min^{-1} and kept for 4 h. The corundum crucible was covered with a lid to maintain the calcination process in static air. After cooled naturally to room temperature, the obtained powders were grounded and collected, and was labeled as CN.

Graphitic carbon nitride with the rapid high-temperature treatment was prepared as follow. CN (1.0 g) was added into a ceramic crucible with a lid, and then heated up from 20 to 800 °C with a heating rate of 600 °C min^{-1} and kept for 15 min. After cooled to room temperature by circulation cooling water (15 °C), the obtained powders were collected and labeled as CN-800.

2.2. Characterization

X-ray diffraction (XRD) patterns were obtained with a diffractometer (PANalytical X'pert MPD Pro, Netherlands) by a scan rate of 2° min^{-1} in the 2θ range from 10 to 35° under Ni-filtered Cu Kα irradiation. Brunauer-Emmette-Teller (BET) surface area measurement was recorded by an accelerated surface area and porosimetry analyzer (Micromeritics ASAP 2020, USA) with N_2 adsorption analysis. Scanning electron microscopy (SEM) were carried out by a field-emission scanning electron microscope (JEOL JSM-7800F, Japan). Transmission electron microscopy (TEM) were observed by a transmission electron microscope (FEI Tecnai G^2 F30 S-Twin, USA) with an accelerating voltage (300 kV). Fourier transform infrared (FTIR) spectra were measured by an FTIR spectrophotometer (Bruker Vetex70, Germany) with the wavenumber range from 4000 to 400 cm^{-1}. Elemental analysis (EA) was measured by Elemental Analyzer (Elementar vaeeio MACRO cube, Germany). Raman spectra were obtained from a Raman spectrometer (Horiba Lab RAM HR800, Japan) with a laser (33 mW, 325 nm) as excitation source, and the scanned range was from 400 to 2000 cm^{-1}. X-ray photoelectron spectroscopy (XPS) were recorded by an X-ray photoelectron spectroscope (Kratos Axis Ultra DLD, Japan) using a monochromatic Al Kα line source (hν = 1486.69 eV), and the adventitious C 1 s peak at 284.8 eV was applied as reference. UV–Vis spectra were collected by a UV–Vis-near-IR spectrophotometer (Hitachi U-4100, Japan) with $BaSO_4$ reference in the range from 300 to 800 nm. Photoluminescence spectra (PL) were performed by a steady-state fluorescence spectrophotometer (PTI QuantaMaster 40, USA) with an excitation wavelength of 377 nm at room temperature. Electron paramagnetic resonance (EPR) were obtained by a X-band spectrometer (Bruker EMX, A300-9.5/12/S-LC, Germany) at room temperature. Thermogravimetric (TG) curves were obatined by a thermal analyzer (NETZSCH STA 449 C, Germany) in air atmosphere with the range from 50 to 1000 °C.

2.3. Photoelectrochemical measurement

Preparation of photoanodes: As-prepared photocatalyst (5 mg) was added into the mixed solution consisted of deionized water (500 μL), ethanol (500 μL) and Nafion solutions (20 μL, DuPont D1020, 10 wt%), and then kept ultrasonic for 30 min. The suspension (200 μL) was then coated onto cleaned FTO glass (1.0 × 1.5 cm^2), and dried at room temperature overnight. The synthesized photoanodes based on CN and CN-800 were labeled as CN-PA and CN-800-PA, respectively.

Photoelectrochemical properties were measured in a three-electrode cell including a Pt slice as counter electrode, Ag/AgCl as reference electrode and photoanodes as working anode, and Na_2SO_4 (0.5 M, pH = 6.8) aqueous solution as electrolyte. The transient photocurrent densities were recorded with an applied voltage of 0.5 V vs Ag/AgCl, and Mott-Schottky (MS) curves were recorded under dark condition (1 KHz). Meanwhile, electrochemical impedance spectroscopy (EIS) were obtained under visible-light irradiation in the frequency range from 100 KHz to 1 Hz (0.5 V vs Ag/AgCl). The potential vs Ag/AgCl were converted to corresponding potential vs RHE based on the following equation.

$E_{RHE} = E_{Ag/AgCl} + 0.059 \times pH + E^{\circ}_{Ag/AgCl}$ ($E^{\circ}_{Ag/AgCl}$is 0.1976 V at

25 °C) (1)

2.4. Photocatalytic measurement

Photocatalytic measurements for H_2 evolution were performed in a Pyrex glass cell (270 mL) under visible-light irradiation. A 300 W Xe lamp with a UV-cutoff filter ($\lambda > 420$ nm) was applied as the visible-light source. Triethanolamine (TEOA) was used as sacrificial agent to consume photo-generated holes, and Pt as H_2-evolution cocatalyst was loaded on photocatalysts by in-situ photo-deposition from the precursor of $H_2PtCl_6{\cdot}6H_2O$. Typically, photocatalysts (50 mg) was added into TEOA aqueous solutions (10%, 200 mL) with stirring. Then H_2PtCl_6 aqueous solution was added to load Pt cocatalyst (1–5 wt%). After purging with N_2 to eliminate air for 15 min, the suspension was irradiated with stirring at a constant temperature of around 35 °C. The evolved H_2 was analyzed using a gas chromatogram with a TDX-01 column and high-purity Ar as carrier gas.

AQY at 425 nm was measured under the irradiation of 300 W Xe lamp with a band-pass filter (425 nm), and added photocatalysts (50 mg) were loaded with 3 wt% Pt by in-situ photo-deposition. Besides, the intensity of irradiated light was gained from a spectrodiometer (Avantes AvaSpec-2048-USB2, Netherlands). The calculation of AQY was carried out by the following Equation (2):

$$\mathrm{AQY}(\%) = \frac{\text{Number of reacted electrons}}{\text{Number of incident photons}} \times 100 = \frac{\text{Number of evolved } H_2 \text{ molecules} \times 2}{\text{Number of incident photons}} \times 100 \quad (2)$$

3. Results and discussion

XRD patterns for CN and CN-800 are observed from Fig. 1a, in which both samples exhibited the characteristic diffraction peaks of graphitic carbon nitride. For CN, the weak peak at 12.8° belonged to the (100) diffraction peak of graphitic carbon nitride, and was attributed to in-plane repeating units of the continuous heptazine framework. Meanwhile, the peak at around 27.3° due to the (002) diffraction peak of graphitic carbon nitride was assigned to the stacking of the conjugated aromatic structure, that is carbon nitride sheets [32–34]. The intensity ratios of (100) and (002) diffraction peaks for CN and CN-800 were 0.12 and 0.07, respectively, indicating that the (100) diffraction peak became weaker after the rapid high-temperature treatment. It meant that the in-plane structure of the continuous heptazine framework by the rapid high-temperature treatment was suffered from some extent of destruction. Moreover, with the rapid high-temperature treatment, the (002) diffraction peak became narrower, and obviously shifted to high angle, implying that the internal distance of stacked adjacent carbon nitride sheets decreased. As reported, the single layers of bulk graphitic carbon nitride are potentially undulated, but could be planarized with further heat treatment, resulting in narrower width of the (002) peak and denser stacking [16,35]. Then it was speculated that the change of (002) diffraction peak could be assigned to the process of rapid high-temperature treatment. UV–vis spectra and corresponding band gap energies for CN and CN-800 are shown in Fig. 1b. CN showed a visible absorption edge at 470 nm corresponding to its band gap (2.64 eV) [6,13,36], and the absorption edge of CN-800 was located at 441 nm corresponding to band gap of 2.81 eV. Therefore, with the rapid high-temperature treatment, the absorption edge of graphitic carbon nitride had an obvious blue-shift. Meanwhile, the wide background absorption (500–600 nm) was also seen in CN-800, implying that the absorption for visible light, especially the near-infrared light, could be greatly enhanced by the rapid high-temperature treatment.

Figs. 2 and S2 show nitrogen absorption-desorption isotherms and corresponding pore size distribution curves of CN and CN-800. It was obviously observed that both samples exhibited the type IV isotherms [37,38]. After the rapid high-temperature treatment, a high adsorption capacity in high relative pressure ($P/P_0 > 0.8$) was obtained from the nitrogen absorption-desorption isotherm of CN-800, indicating the generation of abundant mesopores and macropores [17]. Meanwhile, from Table S1, CN-800 showed a surface area of 60.51 $m^2\,g^{-1}$, which was around 8 times that of CN (7.38 $m^2\,g^{-1}$). As observed from the pore size distribution curves for CN and CN-800 (Fig. 2b), the sharp peak at 2.0 nm due to layer-aggregated pores existed in both samples, and its intensity obviously increased by the rapid high-temperature treatment, implying that denser stacking of graphitic carbon nitride sheets happened in CN-800 corresponding to XRD results. Another distinct peak at 1.4 nm was also seen for CN-800. It was speculated that the treatment not only promoted generation of mesopores, but also brought into plentiful micropores. Meanwhile, the extended wide peak at 3–40 nm for CN-800 (Fig. S2) also confirmed the presence of mesopores [39].

Micromorphologies for CN and CN-800 were obtained by SEM and TEM, which are shown in Fig. 3. CN consisted of the thick bulk with aggregation of carbon nitride 2D sheets (Fig. 3a and d) [5,40,41]. The morphology of graphitic carbon nitride was extremely changed with the rapid high-temperature treatment. The thin sheets with mesopores and macropores and with wrinkles for CN-800 were observed from SEM images (Fig. 3b and c), which was attributed to exfoliation of the aggregated 2D carbon nitride sheets by the process of rapid high-temperature treatment based on porosity analysis. Moreover, the microstructure of thin sheets could be also clearly seen from TEM images of CN-800. The abundant micropores and macropores were generated as circled in Fig. 3f. It was reported that thinner graphitic carbon nitride

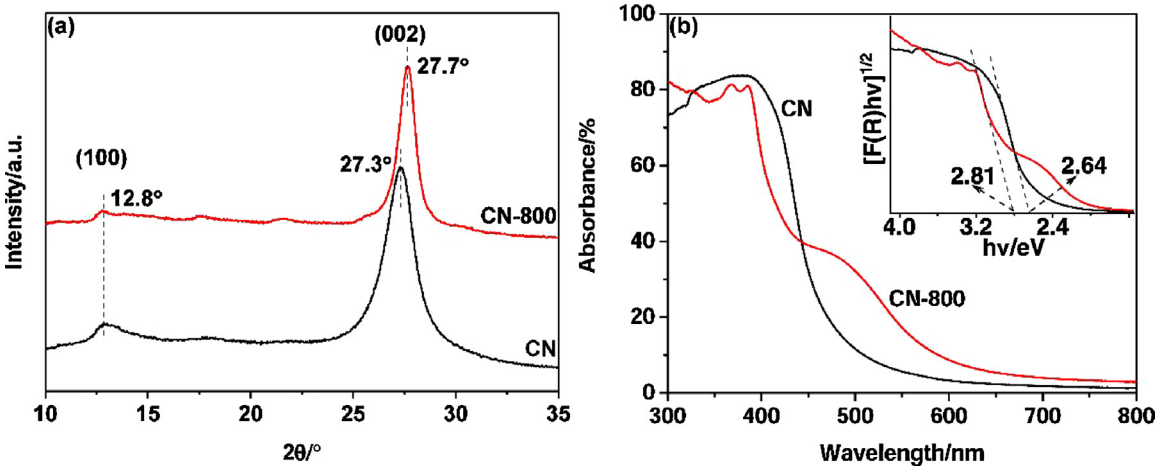

Fig. 1. (a) XRD patterns and (b) UV–vis spectra (inset, band gap-energy calculation) for CN and CN-800.

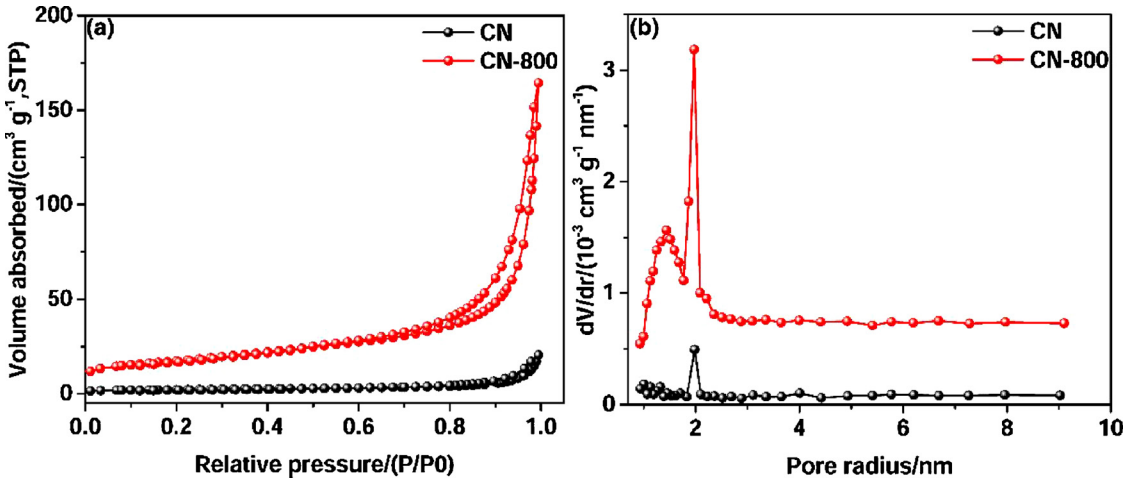

Fig. 2. (a) Nitrogen absorption-desorption isotherms and (b) corresponding pore size distribution curves (1–9 nm) for CN and CN-800.

sheets led to the increase of its band gap due to quantum confinement effect [16,17,42,43]. Therefore, the blue-shift of absorption edge for CN-800 compared with that for CN (Fig. 1b) should be attributed to the quantum confinement effect in thinner graphitic carbon nitride sheets generated during the process of rapid thermal treatment.

Table S2 shows the elemental composition for CN and CN-800 by Elemental Analyzer (EA), in which weight ratios of N and C elements slightly decreased with the rapid high-temperature treatment. It was proved that some nitrogen vacancies were generated with the rapid high-temperature treatment. FTIR spectra for CN and CN-800 are shown in Figs. 4a and b and S3. As for CN, the peak at 3500–3100 cm^{-1} was assigned to the vibrational absorption of N—H and O—H, while the peaks in the range from 1600 to 1200 cm^{-1} were due to aromatic C—N heterocyclic units (Fig. S3) [12,33,44,45]. Moreover, the peak at 807 cm^{-1} was ascribed to the bending mode of heptazine rings, implying the presence of the basic melon units with NH/NH$_2$ groups [12,44,46,47]. Three new peaks at 1277, 1334 and 1430 cm^{-1} appeared in CN-800 (Fig. 4a), which indicated that the rapid high-temperature treatment changed the structure of C–N heterocyclic units in graphitic carbon nitride. Meanwhile, for CN-800, the peak at 811 cm^{-1} due to the bending of heptazine rings, shifted to higher wavenumber compared with that for CN (Fig. 4b), which might be attributed to the generated nitrogen vacancies based on EA result [48]. Meanwhile, the presence of nitrogen vacancies in graphitic carbon nitride could promote its absorption for visible light with long wavelength [49,50]. The wide background absorption of CN-800 for visible light (500–600 nm) from UV–vis result further proved generation of nitrogen vacancies in the rapid thermal process under high temperature. Fig. 4c shows Raman spectra for CN and CN-800, in which the peaks at 704 and 974 cm^{-1} were attributed to the breathing modes of trizine rings [51–55]. Another peak at 752 cm^{-1} for CN belonged to the out-of-plane bending mode of graphitic domains in graphitic carbon nitride [51–54], and shifted to higher wavenumbers compared with that of the corresponding peak (763 cm^{-1}) for CN-800, further implying that the structure of graphitic carbon nitride was changed by the rapid high-temperature treatment. Moreover, EPR spectra (Fig. 4d) showed that both CN and CN-800 had one single Lorentzian line, which was assigned to the unpaired electron by the carbon atoms of the aromatic rings within π-bonded nanosized clusters [46,56,57]. The stronger spin intensity for CN-800 than that for CN proved that the rapid high-temperature treatment promoted generation of more unpaired electrons, further indicating structure change of graphitic carbon nitride

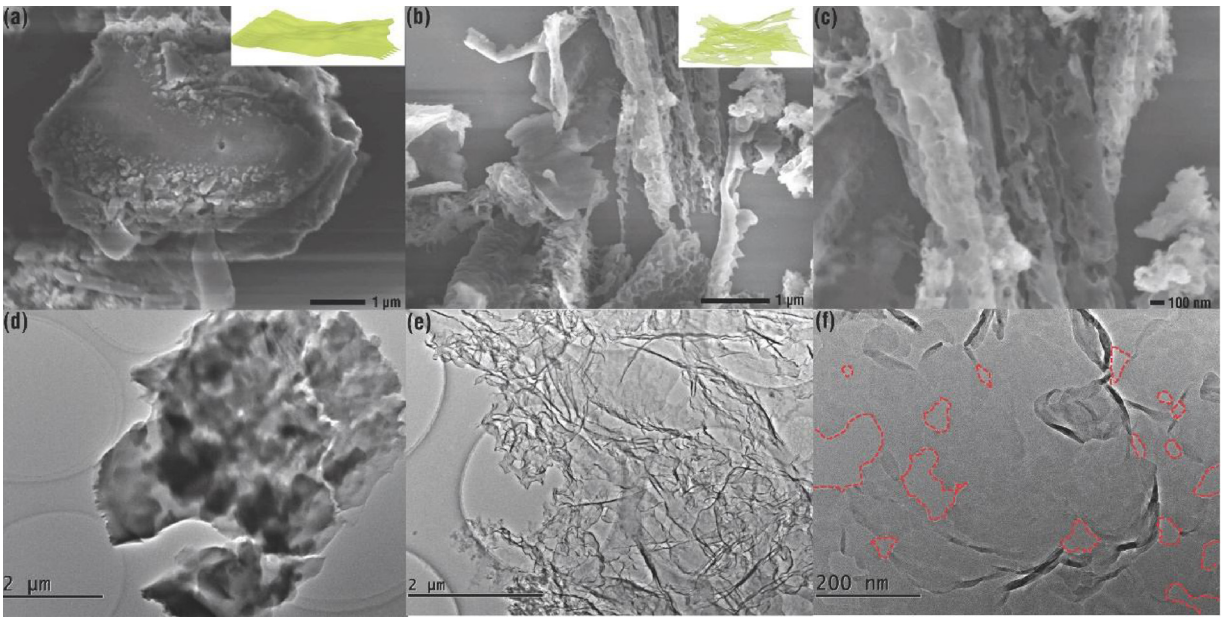

Fig. 3. SEM and TEM images for CN (a, d) and CN-800 (b, c, e, f). Scale bar: (a, b) 1 μm, (c) 100 nm, (d, e) 2 μm, (f) 200 nm.

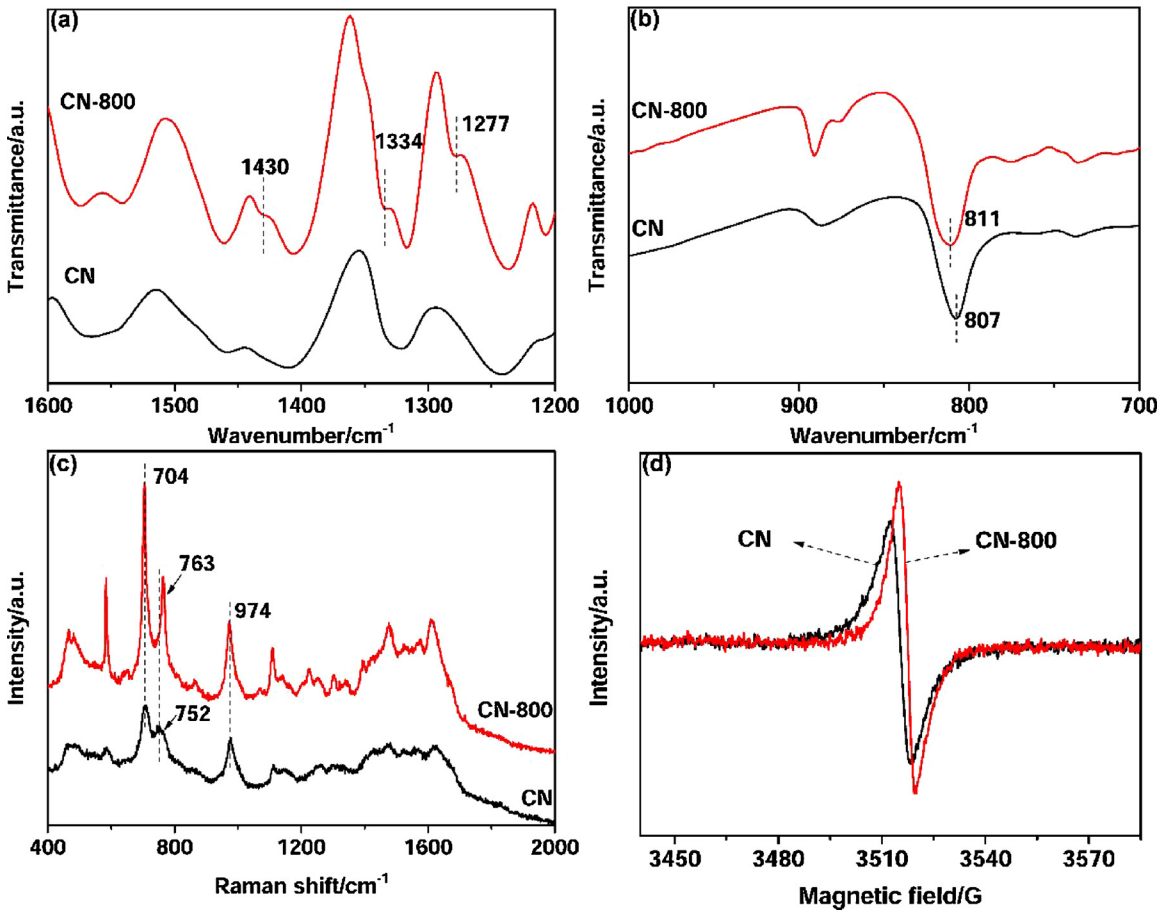

Fig. 4. (a, b) FTIR spectra, (c) Raman spectra and EPR spectra for CN and CN-800.

corresponding to XRD, FTIR, and Raman analysis [46,48,56].

XPS wide spectra (Fig. S4) showed that there were only C, N and O elements in CN and CN-800, and the existence of O was attributed to the surface absorbed water. As observed from C 1 s spectra (Fig. 5a), CN showed three peaks at 284.8, 286.0 and 288.1 eV (Table S3), which were due to the graphitic carbon (C═C), C═N and sp^2-hybridized carbon in the N-containing aromatic ring (N═C−N), respectively [39,40,58]. After the rapid high-temperature treatment, the peak of C═N slightly shifted to low binding energy, which was assigned to the formed N vacancies based on UV–vis, EA and FTIR results. The content ratio between C species of C═N and N═C−N increased, and thereby the contents of N═C−N should decrease (Table S3), which implied that the formed N vacancies might be located at the positions of N in C−N heterocyclic units. For N 1 s spectra of CN (Fig. 5b), there were four peaks at 398.4, 399.2, 400.7 and 404.0 eV, corresponding to sp^2-hybridized nitrogen in triazine rings (C−N═C), tertiary nitrogen N-$(C)_3$ groups, amino functions carrying hydrogen (N−H) and π excitation, respectively [12,39,59]. It was found that the peak of N-$(C)_3$ for CN-800 shifted to low binding energy compared with that of CN, which was attributed to the structure change of graphitic carbon nitride. Meanwhile, the content ratio between N species of C−N═C and N-$(C)_3$ decreased by the rapid high-temperature process, further proving that the formed N vacancies belonged to N in C−N heterocyclic units. Besides, from Fig. S5 and Table S3, no obvious change for O 1 s spectra of CN and CN-800 could be observed. As shown in Fig. 5c, the deduced valence band maximum (VBM) values for CN and CN-800 were around 1.98 and 1.90 eV (vs. the Fermi level (EF)), respectively, thus indicating that the VBM of CN-800 was 0.08 eV more negative than that of CN. Combined with the UV–vis result, the conduction band minimum (CBM) of CN-800 was 0.25 eV more negative than that of CN, and the illustration of their band structures is shown in Fig. 5d.

Fig. 6 shows PL spectra for CN and CN-800. It was indicated that the intensity of photoluminescence for CN-800 was extremely lower than that for CN, thereby implying that the recombination of photo-generated carriers was greatly inhibited after the rapid high-temperature treatment [12,17,39].

Photocatalytic H_2-evolution activities for CN and CN-800 are shown in Fig. 7a. The photocatalytic activity of CN-800 was up to 892.8 μmol h^{-1} $g_{cat}{}^{-1}$, which was 25.5 times that of CN (35 μmol h^{-1} $g_{cat}{}^{-1}$), implying that the rapid high-temperature treatment as one of effective methods could greatly improve photocatalytic performance of graphitic carbon nitride. The enhancement factor by the rapid high-temperature treatment vs. bulk graphitic carbon nitride is much higher than that from most of previous graphitic carbon nitride photocatalysts with exfoliation or micromorphology modification in recent years (Table S4). Moreover, Fig. S6 shows photocatalytic activities of graphitic carbon nitride with different holding times, resulting that their photocatalytic activities increased with longer holding time, and the optimum holding time is 15 min corresponding to the sample of CN-800. CN-800 showed the highest photocatalytic activity (1381.0 μmol h^{-1} $g_{cat}{}^{-1}$) with loading 3 wt% Pt cocatalyst (Fig. S7a), and the apparent quantum yield (AQY) at 425 nm was up to 6.84%. Besides, photocatalytic activity for CN-800 had no obvious decrease in the photocatalytic measurement of 21 h (Fig. S7b), proving its favorable photocatalytic stability.

Furthermore, photoeletrochemical properties of CN-PA and CN-800-PA were analyzed to deeply explore the mechanism of enhanced photocatalytic ability by the rapid high-temperature treatment. By comparison of the photocurrent densities in Fig. 7b, CN-800-PA showed better photoelectrochemical performance than CN-PA, further implying

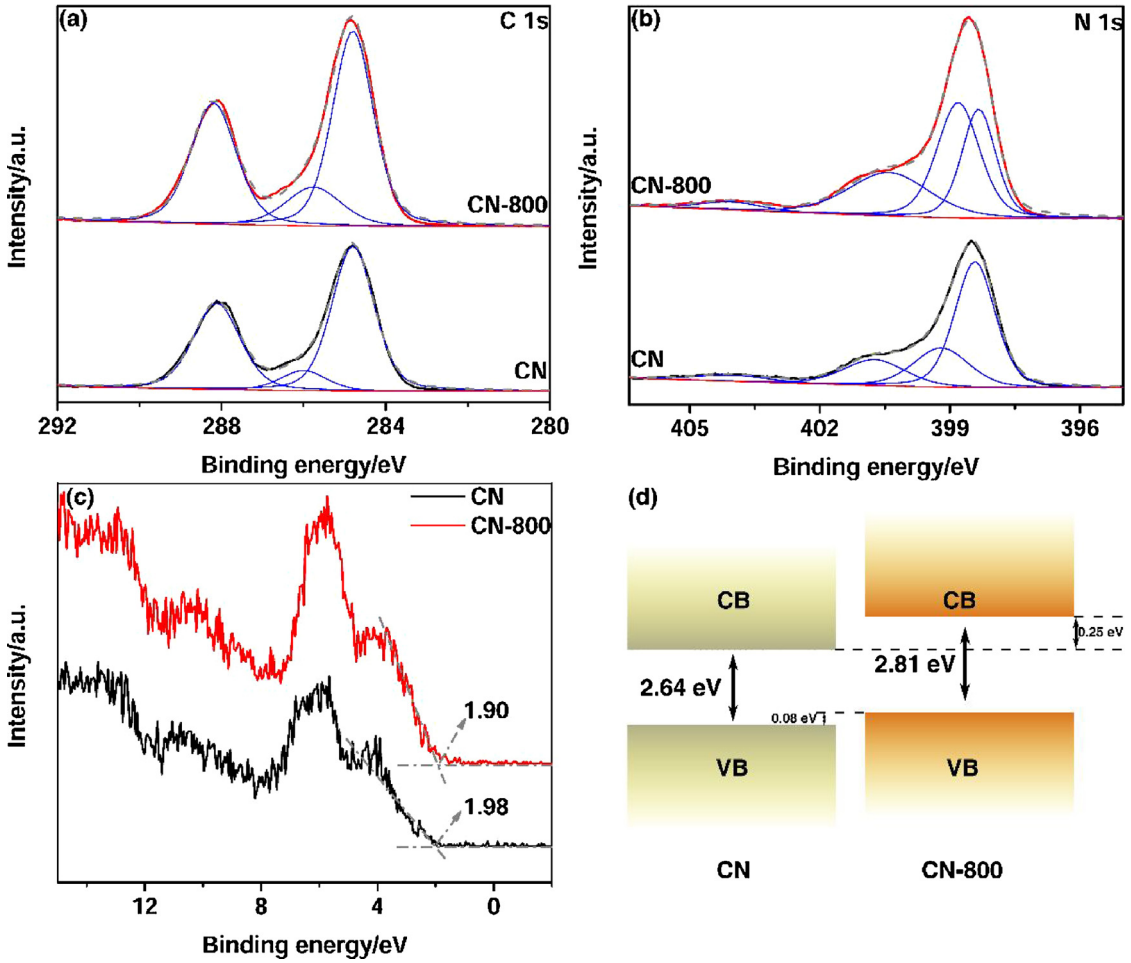

Fig. 5. XPS (a) C 1 s, (b) N 1 s and (c) VB spectra, (d) illustration of band structures for CN and CN-800.

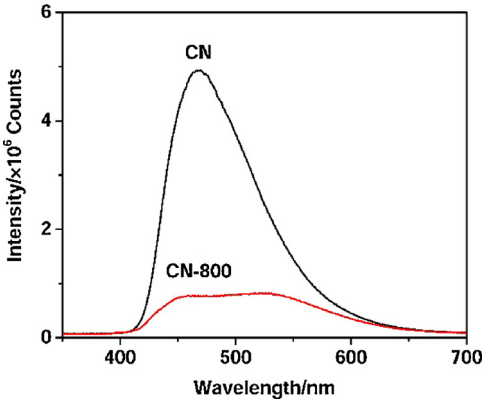

Fig. 6. PL spectra for CN and CN-800.

the effective modification of rapid high-temperature treatment on graphitic carbon nitride. It was observed from Mott-Schottky plots (Fig. 7c) that CN-800-PA had much smaller slope than CN-PA, proving higher donor concentrations in CN-800-PA, and higher donor concentrations should be assigned to generation of N vacancies corresponding to UV–vis, FTIR, EA and XPS results [60]. Meanwhile, CN-800-PA had more negative flat-band potential compared with CN-PA corresponding to XPS result. EIS in Fig. 7d showed that CN-800-PA had an arc with smaller radius than that of CN-PA, indicating more effective interface charge transport and effective separation of photo-generated carriers after the rapid high-temperature treatment corresponding to PL analysis [12,17,61–63]. Besides, as observed from Fig. S8 (detailed preparation and characterization of electrolytes in Experimental section in Supporting Information), comparing with CN-ET, CN-800-ET showed better electrochemical ability for hydrogen water reduction (HER) after the rapid high-temperature treatment, implying that HER ability of graphitic carbon nitride could be also improved by the rapid high-temperature treatment.

According to the above analysis, the rapid high-temperature treatment can be considered as one efficient method to improve photocatalytic H_2-evolution performance of graphitic carbon nitride. Firstly, the microstructure of graphitic carbon nitride is greatly modified, and the porous and thin g-C_3N_4 sheets with wrinkles are generated based on SEM and TEM results. Then the microstructure change effectively increases BET surface areas of graphitic carbon nitride, thereby leading that more active sites could be provided for photocatalytic H_2-evolution reaction. Secondly, due to the quantum confinement effect of thinner graphitic carbon nitride sheets and the generated nitrogen vacancies in C—N heterocyclic units, the electronic structure properties of graphitic carbon nitride are changed, which brings favorable influence on generation, separation and transfer of photo-generated carriers [16,17,49,50]. More photo-generated carriers are produced based on the enhanced absorption for visible light (up to 600 nm), and the separation and transfer of photo-generated carriers is greatly enhanced based on PL and EIS results. Moreover, stronger driving force for photocatalytic H_2-evolution reaction is obtained to enhance the ability of water reduction reaction based on XPS and Mott-Schottky results.

4. Conclusion

A rapid high-temperature treatment method was developed to

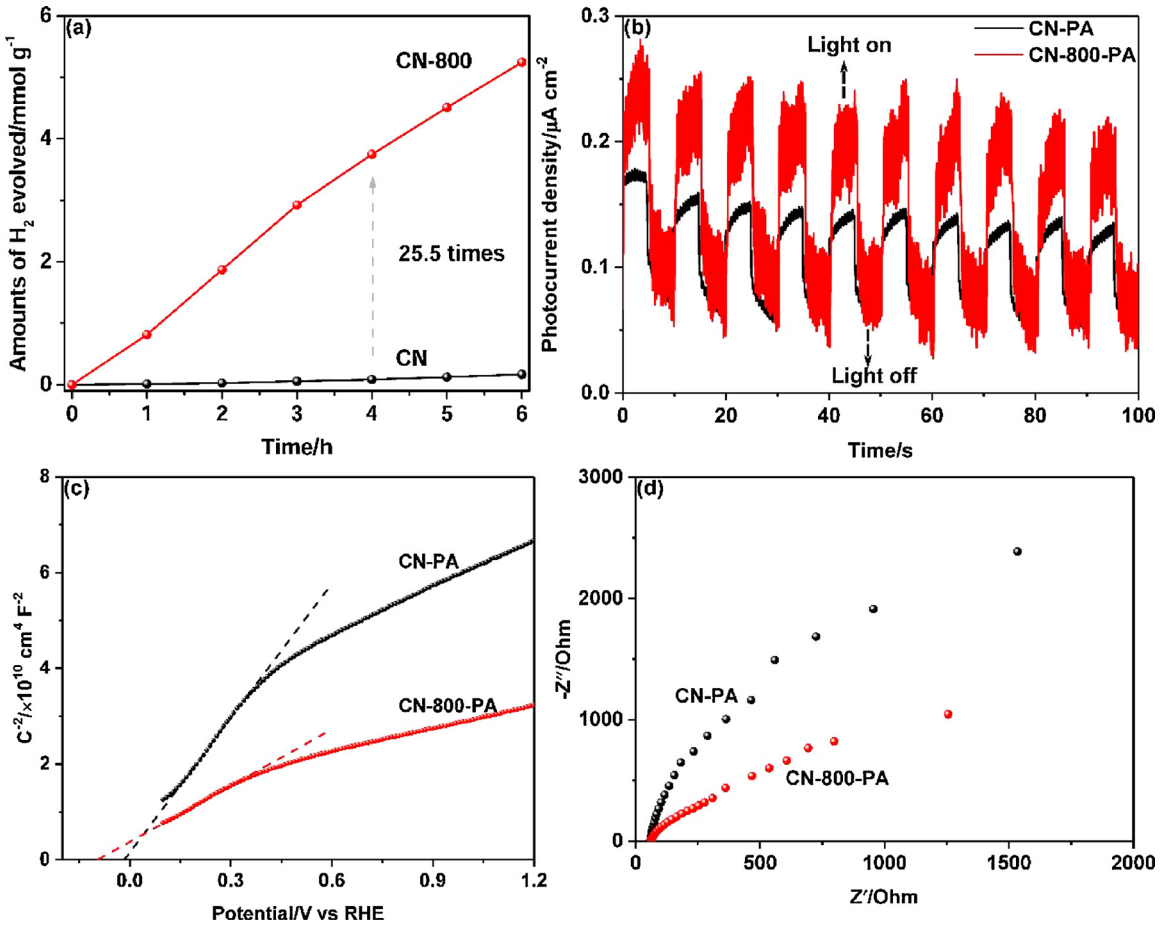

Fig. 7. (a) Photocatalytic H_2-evolution activities for CN and CN-800; (b) Transient photocurrent densities, (c) Mott-Schottky plots and (d) Electrochemical Impedance Spectroscopy (EIS) for CN-PA and CN-800-PA.

realize effective modification on pristine graphitic carbon nitride, achieving greatly enhanced (25.5 times) visible-light photocatalytic H_2-evolution performance. It was found that, the significant increase of surface areas provided more active sites for photocatalytic reaction and the thinner graphitic carbon nitride sheets and the generated nitrogen vacancies in C—N heterocyclic units effectively improved the generation, separation and transfer of photo-generated carriers. Meanwhile, the stronger driving force for photocatalytic H_2-evolution reaction enhanced the ability of photocatalytic water reduction reaction. This work presents a promising modification strategy for graphitic carbon nitride as a typical example of two-dimension materials for photocatalysis and related potential application.

Acknowledgements

This work is supported by the National Natural Science Foundation of China (Nos. 51302212 and 21606175), the China Postdoctoral Science Foundation (Nos. 2014T70915 and 2013M540745), the Postdoctoral Science Foundation in Shaanxi Province of China, the Natural Science Basic Research Plan in Shaanxi Province of China (No. 2014JQ2-5022), and the Fundamental Research Funds for the Central Universities.

Appendix A. Supplementary data

Supplementary material related to this article can be found, in the online version, at doi:https://doi.org/10.1016/j.apcatb.2018.03.104.

References

[1] X. Chen, S. Shen, L. Guo, S.S. Mao, Chem. Rev. 110 (2010) 6503–6570.
[2] A. Kudo, Y. Miseki, Chem. Soc. Rev. 38 (2009) 253–278.
[3] J. Low, J. Yu, M. Jaroniec, S. Wageh, A.A. Al-Ghamdi, Adv. Mater. 29 (2017) 1601694.
[4] X. Wang, K. Maeda, A. Thomas, K. Takanabe, G. Xin, J.M. Carlsson, K. Domen, M. Antonietti, Nat. Mater. 8 (2009) 76–80.
[5] F.K. Kessler, Y. Zheng, D. Schwarz, C. Merschjann, W. Schnick, X. Wang, M.J. Bojdys, Nat. Rev. Mater. 2 (2017) 17030.
[6] G. Zhang, Z.A. Lan, X. Wang, Angew. Chem. Int. Ed. 55 (2016) 15712–15727.
[7] X. Wang, K. Maeda, X. Chen, K. Takanabe, K. Domen, Y. Hou, X. Fu, M. Antonietti, J. Am. Chem. Soc. 131 (2009) 1680–1681.
[8] J. Liu, Y. Liu, N.Y. Liu, Y.Z. Han, X. Zhang, H. Huang, Y. Lifshitz, S.T. Lee, J. Zhong, Z.H. Kang, Science 347 (2015) 970–974.
[9] J. Chen, C.L. Dong, D.M. Zhao, Y.C. Huang, X.X. Wang, L. Samad, L.N. Dang, M. Shearer, S.H. Shen, L.J. Guo, Adv. Mater. 29 (2017) 1606198.
[10] S. Cao, J. Low, J. Yu, M. Jaroniec, Adv. Mater. 27 (2015) 2150–2176.
[11] Z. Zhao, Y. Sun, F. Dong, Nanoscale 7 (2015) 15–37.
[12] Q. Liang, Z. Li, X. Yu, Z.H. Huang, F. Kang, Q.H. Yang, Adv. Mater. 27 (2015) 4634–4639.
[13] K.S. Lakhi, D.-H. Park, K. Al-Bahily, W. Cha, B. Viswanathan, J.-H. Choy, A. Vinu, Chem. Soc. Rev. 46 (2017) 560-560.
[14] Q. Han, N. Chen, J. Zhang, L. Qu, Mater. Horiz. 4 (2017) 832–850.
[15] T. Sano, S. Tsutsui, K. Koike, T. Hirakawa, Y. Teramoto, N. Negishi, K. Takeuchi, J. Mater. Chem. A 1 (2013) 6489–6496.
[16] P. Niu, L. Zhang, G. Liu, H.M. Cheng, Adv. Funct. Mater. 22 (2012) 4763–4770.
[17] Y. Li, R. Jin, Y. Xing, J. Li, S. Song, X. Liu, M. Li, R. Jin, Adv. Energy Mater. 6 (2016) 1601273.
[18] M.J. Bojdys, N. Severin, J.P. Rabe, A.I. Cooper, A. Thomas, M. Antonietti, Macromol. Rapid Commun. 34 (2013) 850–854.
[19] X. She, H. Xu, Y. Xu, J. Yan, J. Xia, L. Xu, Y. Song, Y. Jiang, Q. Zhang, H. Li, J. Mater. Chem. A 2 (2014) 2563–2570.
[20] H. Xu, J. Yan, X. She, L. Xu, J. Xia, Y. Xu, Y. Song, L. Huang, H. Li, Nanoscale 6 (2014) 1406–1415.
[21] H. Zhao, H. Yu, X. Quan, S. Chen, Y. Zhang, H. Zhao, H. Wang, Appl. Catal. B: Environ. 152 (2014) 46–50.

[22] J. Hong, S. Yin, Y. Pan, J. Han, T. Zhou, R. Xu, Nanoscale 6 (2014) 14984–14990.
[23] D.R. Dreyer, A.D. Todd, C.W. Bielawski, Chem. Soc. Rev. 43 (2014) 5288–5301.
[24] Z. Jin, J.R. Lomeda, B.K. Price, W. Lu, Y. Zhu, J.M. Tour, Chem. Mater. 21 (2009) 3045–3047.
[25] R. Raccichini, A. Varzi, S. Passerini, B. Scrosati, Nat. Mater. 14 (2015) 271–279.
[26] Y. Sun, Q. Wu, G. Shi, Energy Environ. Sci. 4 (2011) 1113–1132.
[27] Y. Qiu, S. Moore, R. Hurt, I. Külaots, Carbon 111 (2017) 651–657.
[28] M.J. McAllister, J.-L. Li, D.H. Adamson, H.C. Schniepp, A.A. Abdala, J. Liu, M. Herrera-Alonso, D.L. Milius, R. Car, R.K. Prud'homme, Chem. Mater. 19 (2007) 4396–4404.
[29] M. Acik, G. Lee, C. Mattevi, M. Chhowalla, K. Cho, Y. Chabal, Nat. Mater. 9 (2010) 840–845.
[30] A. Thomas, A. Fischer, F. Goettmann, M. Antonietti, J.-O. Müller, R. Schlögl, J.M. Carlsson, J. Mater. Chem. 18 (2008) 4893–4908.
[31] X. Wang, S. Blechert, M. Antonietti, ACS Catal. 2 (2012) 1596–1606.
[32] X. Chen, H. Chen, J. Guan, J. Zhen, Z. Sun, P. Du, Y. Lu, S. Yang, Nanoscale 9 (2017) 5615–5623.
[33] J. Li, B. Shen, Z. Hong, B. Lin, B. Gao, Y. Chen, Chem. Commun. 48 (2012) 12017–12019.
[34] Z.-F. Huang, J. Song, L. Pan, Z. Wang, X. Zhang, J.-J. Zou, W. Mi, X. Zhang, L. Wang, Nano Energy 12 (2015) 646–656.
[35] M. Groenewolt, M. Antonietti, Adv. Mater. 17 (2005) 1789–1792.
[36] C. Cheng, J. Shi, Y. Hu, L. Guo, Nanotechnology 28 (2017) 164002.
[37] M.K. And, M. Jaroniec, Chem. Mater. 13 (2001) 3169–3183.
[38] J. Yuan, J. Wen, Y. Zhong, X. Li, Y. Fang, S. Zhang, W. Liu, J. Mater. Chem. A 3 (2015) 18244–18255.
[39] M.R. Gholipour, F. Béland, T.-O. Do, ACS Sustainable Chem. Eng. 5 (2016) 213–220.
[40] W. Che, W. Cheng, T. Yao, F. Tang, W. Liu, H. Su, Y. Huang, Q. Liu, J. Liu, F. Hu, J. Am. Chem. Soc. 139 (2017) 3021.
[41] J. Shi, C. Cheng, Y. Hu, M. Liu, L. Guo, Int. J. Hydrog. Energy 42 (2017) 4651–4659.
[42] Q. Han, B. Wang, J. Gao, Z. Cheng, Y. Zhao, Z. Zhang, L. Qu, ACS Nano 10 (2016) 2745–2751.
[43] J. Xu, L. Zhang, R. Shi, Y. Zhu, J. Mater. Chem. A 1 (2013) 14766–14772.
[44] Y. Kang, Y. Yang, L.C. Yin, X. Kang, G. Liu, H.M. Cheng, Adv. Mater. 27 (2015) 4572–4577.
[45] X. She, J. Wu, J. Zhong, H. Xu, Y. Yang, R. Vajtai, J. Lou, Y. Liu, D. Du, H. Li, Nano Energy 27 (2016) 138–146.
[46] G. Liu, G. Zhao, W. Zhou, Y. Liu, H. Pang, H. Zhang, D. Hao, X. Meng, P. Li, T. Kako, Adv. Funct. Mater. 26 (2016) 6822–6829.
[47] K. Li, X. Xie, W.D. Zhang, ChemCatChem 8 (2016) 2128–2135.
[48] C.-Q. Xu, K. Li, W.-D. Zhang, J. Colloid Interface Sci. 495 (2017) 27–36.
[49] P. Niu, L.C. Yin, Y.Q. Yang, G. Liu, H.M. Cheng, Adv. Mater. 26 (2014) 8046–8052.
[50] H. Yu, R. Shi, Y. Zhao, T. Bian, Y. Zhao, C. Zhou, W. Gin, L.Z. Wu, C.H. Tung, T. Zhang, Adv. Mater. 29 (2017) 1605148.
[51] Q. Han, B. Wang, J. Gao, L. Qu, Angew. Chem. 128 (2016) 11007–11011.
[52] M. Wu, J.M. Yan, Xn. Tang, M. Zhao, Q. Jiang, ChemSusChem 7 (2014) 2654–2658.
[53] B. Long, J. Lin, X. Wang, J. Mater. Chem. A 2 (2014) 2942–2951.
[54] A.B. Jorge, D.J. Martin, M.T. Dhanoa, A.S. Rahman, N. Makwana, J. Tang, A. Sella, F. Corà, S. Firth, J.A. Darr, J. Phys. Chem. C 117 (2013) 7178–7185.
[55] Y. Wang, M.K. Bayazit, S. Moniz, Q. Ruan, C.L. Chi, N. Martsinovich, J. Tang, Energy Environ. Sci. 10 (2017) 1643–1651.
[56] Y. Zheng, L. Lin, X. Ye, F. Guo, X. Wang, Angew. Chem. 126 (2014) 12120–12124.
[57] J. Zhang, M. Zhang, R.Q. Sun, X. Wang, Angew. Chem. 124 (2012) 10292–10296.
[58] Y. Zeng, C. Liu, L. Wang, S. Zhang, Y. Ding, Y. Xu, Y. Liu, S. Luo, J. Mater. Chem. A 4 (2016) 19003–19010.
[59] S. Guo, Z. Deng, M. Li, B. Jiang, C. Tian, Q. Pan, H. Fu, Angew. Chem. Int. Ed. 55 (2016) 1830–1834.
[60] R. Franking, L. Li, M.A. Lukowski, F. Meng, Y. Tan, R.J. Hamers, S. Jin, Energy Environ. Sci. 6 (2013) 500–512.
[61] A. Zada, M. Humayun, F. Raziq, X. Zhang, Y. Qu, L. Bai, C. Qin, L. Jing, H. Fu, Adv. Energy Mater. 6 (2016) 1601190.
[62] X. Bai, R. Zong, C. Li, D. Liu, Y. Liu, Y. Zhu, Appl. Catal. B: Environ. 147 (2014) 82–91.
[63] Y. Zhang, J. Shi, C. Cheng, S. Zong, J. Geng, X. Guan, L. Guo, Appl. Catal. B: Environ. (2018), http://dx.doi.org/10.1016/j.apcatb.2018.03.067.